

**Sophie Leanza**<sup>1</sup>

Department of Mechanical Engineering,  
Stanford University,  
Stanford, CA 94305;  
Department of Mechanical and Aerospace  
Engineering,  
The Ohio State University,  
Columbus, OH 43210  
e-mails: leanza@stanford.edu;  
leanza.13@osu.edu

**Shuai Wu**<sup>1</sup>

Department of Mechanical Engineering,  
Stanford University,  
Stanford, CA 94305  
e-mail: shuaiwu@stanford.edu

**Jize Dai**<sup>1</sup>

Department of Mechanical Engineering,  
Stanford University,  
Stanford, CA 94305;  
Department of Mechanical and Aerospace  
Engineering,  
The Ohio State University,  
Columbus, OH 43210  
e-mail: dai.491@osu.edu

**Ruike Renee Zhao**<sup>2</sup>

Department of Mechanical Engineering,  
Stanford University,  
Stanford, CA 94305  
e-mail: rrvzhao@stanford.edu

# Hexagonal Ring Origami Assemblies: Foldable Functional Structures With Extreme Packing

*Foldable structures have been of great interest due to their ability to reduce in size from deployed to folded state, enabling easier storage in scenarios with space constraints such as aerospace and medical applications. Hexagonal structural components have been of interest, due to their ability to tessellate, or cover without gap, 2D and 3D surfaces. However, the study on effective folding strategies for hexagon-based structures and the hexagon geometry itself is limited. Here, we report a strategy of snap-folding hexagonal rings, to result in folded states with only 10.6% the initial area of a single ring. Motivated by this significant packing, we utilize a combination of experiments and finite element analysis to study effective folding strategies and packing abilities of various 2D and 3D hexagonal ring assemblies, with structures that can be folded to 1.5% and 0.4% of their initial area and volume, respectively. The effect of geometric parameters of hexagonal rings on the mechanical stability of their assemblies is investigated. Additionally, the instabilities of rings can be utilized to facilitate the automatic deployment of folded ring assemblies under small perturbations. Furthermore, an assembly with rigid functional panels is explored to demonstrate the functionality and design space for hexagonal ring assemblies. With such significant demonstrated area and volume changes upon snap-folding, it is anticipated that hexagonal ring assemblies could inspire future aerospace or biomedical designs, where reconfiguration and large packing are required.*

[DOI: 10.1115/1.4054693]

**Keywords:** hexagonal ring origami, tessellation, foldable structures, deployable structures, buckling instability, packing

## Introduction

Foldable and deployable structures have been studied intensively due to their capability of shape reconfiguration and size reduction, which aid in engineering applications where reconfiguration or space-saving is critical. Pertinent examples include aerospace structures [1,2] and medical stents [3]. Most often, these applications require functionality at the deployed state and storage or transportation at the folded state. The latter can be enhanced by structures that can reduce in size immensely. The benefits of space-saving and reconfiguration are also applicable in areas such as soft robotics [4,5], metamaterials [6–9], and architecture [10,11]. In designing foldable structures, origami and kirigami [12,13], stimuli-responsive materials [14–16], and buckling mechanisms [17,18] have been explored as common strategies. Many foldable/deployable structures are composed of repeated components or tessellations (gapless covering of a surface with repetitive patterns), which have involved origami-based structures [3,13,19] and metamaterials [20–22]. Other examples of deployable tessellations can be seen in space applications such as solar antennas [23] and markedly the James Webb Telescope [24] (Fig. 1(a), [25,26]). The hexagon is an especially intriguing geometrical building block for foldable structures, as it can be tessellated in 2D and 3D space [27] and has the largest area to perimeter ratio among regular polygons that are capable of tessellation by themselves only. Thus, hexagons bring forth the opportunity of close-packed components for foldable structures with optimized material

usage. Although reconfigurable hexagon-based structures have been explored [28–34], there is still limited study on the folding of the hexagon geometry itself to enable much-enhanced packing ratios of these structures.

Recently, ring origami has been demonstrated as a method to fold thin ring-shaped structures into much smaller overlapping geometries [35]. These rings, including those with circular, elliptical, triangular, and rectangular ring shapes, undergo a snap-folding mechanism due to a buckling instability upon bending or twisting loads to result in self-guided folding to stable states with smaller final area. The folded state of each ring consists of three loops, with the circular one having fully overlapping loops and the best packing ratio (folds to 11% of its initial area) compared to other geometries. Assemblies of these rings result in even more significant packing ratios upon stacking and folding. Although triangular and rectangular rings are capable of 2D and 3D tessellation, they fail to fold into fully overlapping loops, which leads to inefficiently packed states with areas that are 25.0% (Fig. 1(b)) and 33.0%, respectively, of their initial areas (See Fig. S1 available in the Supplemental Materials on the ASME Digital Collection for details on triangular ring origami).

To obtain a fully overlapping folded configuration for maximum packing ratio, the polygonal ring needs to have an edge number of  $3n$ , where integer  $n \geq 2$ . This optimized packing is due to the three overlapping loops of the folded configuration. While the hexagonal, nonagonal, and dodecagonal rings all have efficient packing ratios (Fig. 1(b); 10.6%, 10.8%, and 10.8% of their deployed areas, respectively), only the hexagons can tessellate by themselves (Fig. 1(c)); nonagons and dodecagons are not capable of tessellation by themselves, as their repetitive patterns cannot cover a surface without gap (Fig. 1(c)). Figure 1(d) illustrates the benefits of hexagonal ring assemblies via a simple stacking and folding process of 3D

<sup>1</sup>These authors contributed equally to this work.

<sup>2</sup>Corresponding author.

Contributed by the Applied Mechanics Division of ASME for publication in the JOURNAL OF APPLIED MECHANICS. Manuscript received April 6, 2022; final manuscript received May 26, 2022; published online June 21, 2022. Assoc. Editor: Yihui Zhang.

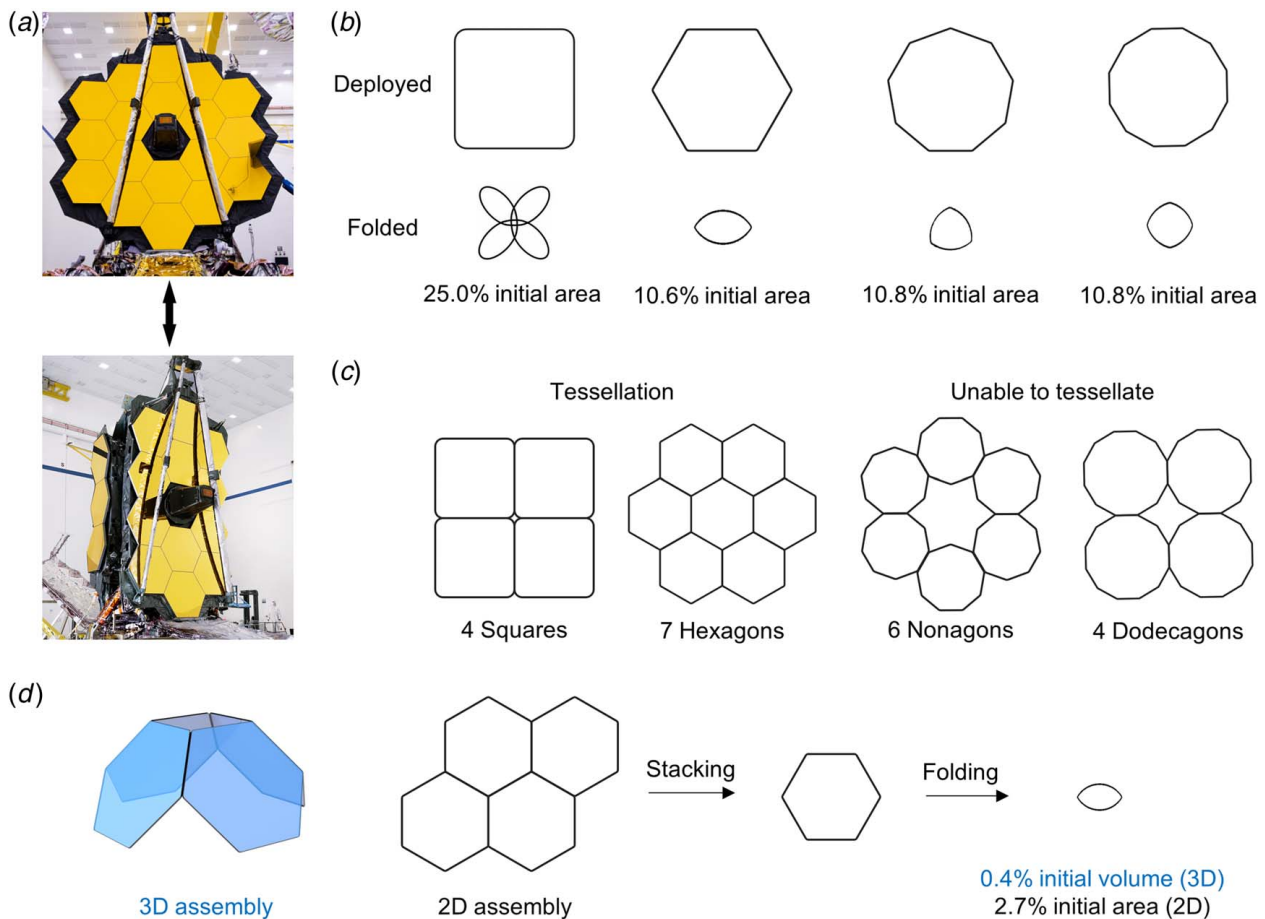


**Fig. 1 Ring origami and tessellation for 2D and 3D ring assemblies with large packing ratios. (a) The James Webb Telescope, a reconfigurable hexagon-tessellated mirror. Top image: Northrop Grumman, NASA/Chris Gunn [25]. Bottom image: NASA/Chris Gunn [26]. (b) deployed and folded states of square, hexagonal, nonagonal, and dodecagonal rings, with their area packing capabilities, (c) 2D tessellation capabilities of squares, hexagons, nonagons, and dodecagons, and (d) examples of 3D and 2D assemblies of four hexagonal rings with the extreme area and volume packing.**

and 2D four-ring assemblies, which results in folded states with 0.4% and 2.7% initial volume and area, respectively, revealing their versatility in structural design and impressive packing capabilities.

Motivated by the large packing and efficient tessellation capabilities exhibited by hexagonal rings, we explore foldable and deployable functional assemblies of hexagonal rings for extreme packing via a combination of experiments and finite element analysis (FEA). We first show the snap-folding process of an individual hexagonal ring when bending or twisting loads are applied, which results in the fully overlapping folded state. We then use the hexagonal ring as a building block for larger 2D and 3D assemblies that can be stacked to overlapping hexagonal rings and then folded. Next, more efficient loading methods are explored to directly fold different complex 3D structures to smaller states with greatly reduced volume, broadening the versatility of designs of hexagonal ring-based assemblies. Additionally, we investigate how the geometric parameters affect the mechanical stability of ring assemblies. Lastly, soft flexible membrane and rigid solar panels are integrated with the hexagonal ring to enhance the functionality of hexagonal ring assemblies. We anticipate that the presented hexagonal ring assemblies will inspire future foldable and deployable engineering designs with outstanding shape and volume change, enabling easier storage and transportation.

## Results

**Snap-Folding of Individual Hexagonal Ring.** The snap-folding of an individual hexagonal ring is first studied (Fig. 2) to

gain insights for the hexagonal ring assemblies (See Materials and Methods and Fig. S2 available in the Supplemental Materials on the ASME Digital Collection for dimensions and fabrication of the ring). The folding can be realized by either twisting or bending, and FEA is utilized to simulate both snap-folding mechanisms. The twisting-induced snap-folding mechanism, as depicted in Fig. 2(a), involves applying a pair of twisting angles (orange arrows) to the left and right corners of the ring. The applied loads are in opposite directions, allowing both corners to rotate about the  $x$ -axis (blue dotted line). The twisting angle at the corners during folding is denoted as  $\Phi$ , with corresponding reaction moment  $M$ . During the folding process, the corners of the ring where twisting angles are applied translate inward along the  $x$ -axis until a twisting angle of  $\pi$  is reached, at which point the ring is fully folded to a stable state of three overlapping loops with the shape that resembles a peach core (Fig. 2(b) and see Movie 1 available in the Supplemental Materials on the ASME Digital Collection). The folded state has an area that is 10.6% of that of the deployed state. The FEA prediction of the twisting-induced snap-folding process of a foldable hexagonal ring is shown in the top row of Fig. 2(b). Experimental results of the snap-folding of a ring with identical dimensions are in the bottom row of Fig. 2(b), demonstrating good agreement with FEA.

The bending-induced snap-folding mechanism, as shown in Fig. 2(c), involves applying a pair of bending angles (orange arrows) in opposing directions to the left and right corners of the ring. The corners rotate about the  $y$ -axis (blue dotted line), with bending angle  $\theta$  at the corners and corresponding reaction

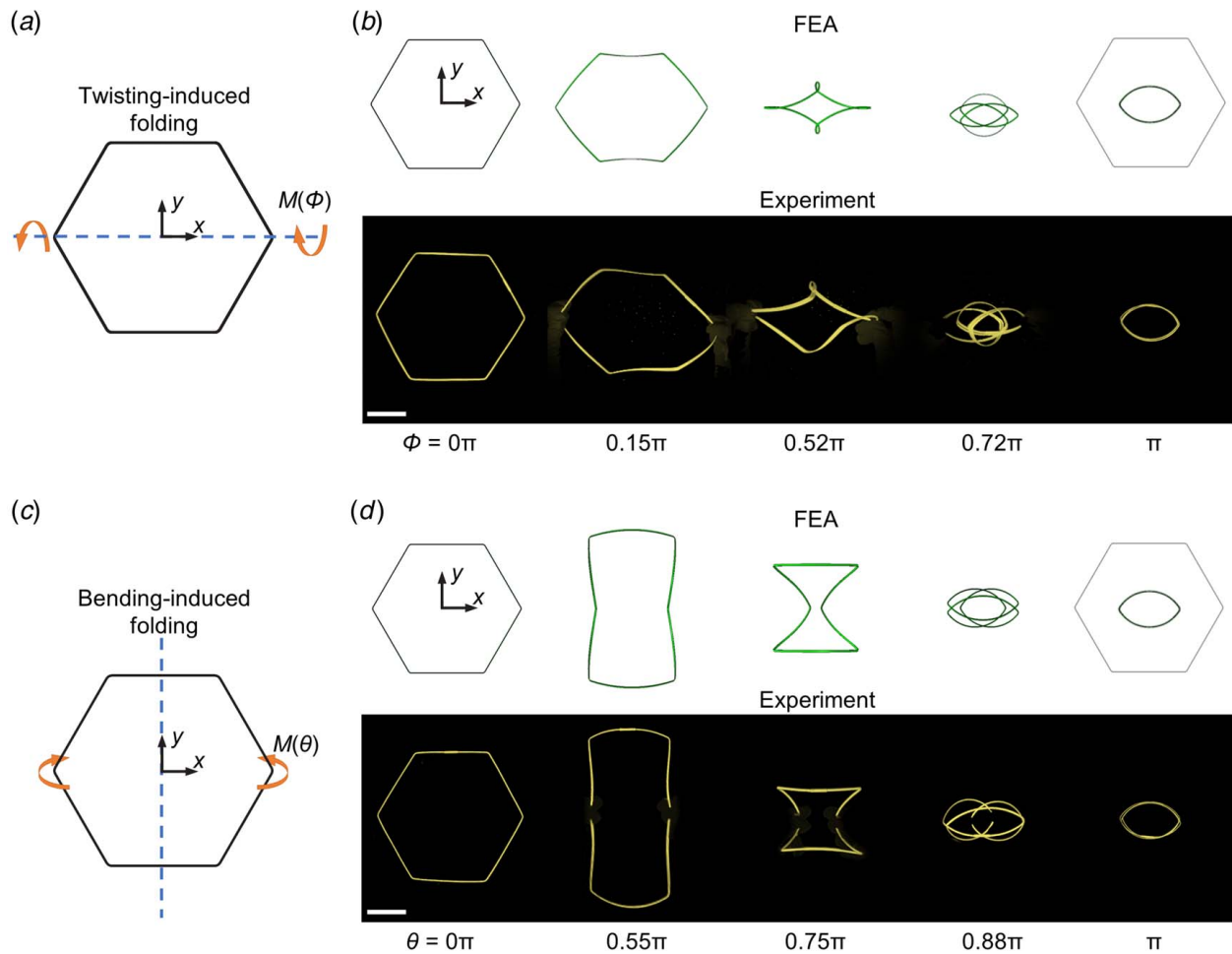


**Fig. 2** FEA simulation and experimental validation of the twisting-induced and bending-induced snap-folding of hexagonal rings. (a) Twisting applied to a hexagonal ring, (b) comparison of FEA and experimental results of folding a hexagonal ring under twisting, (c) bending applied to a hexagonal ring, and (d) comparison of FEA and experimental results of folding a hexagonal ring under bending. Scale bars: 5 cm. (Color version online.)

moment  $M$ . The two corners of the ring with applied loads translate inward along the  $x$ -direction until  $\theta = \pi$ , resulting in the same folded state (Fig. 2(d) and see Movie 1 available in the Supplemental Materials on the ASME Digital Collection). The FEA simulation and the experimental validation of the bending-induced snap-folding process are shown in Fig. 2(d). Note that both folding processes are completely reversible, and the ring can deploy back to its initial state by applying reversed bending or twisting angles to the corners. While the application of either bending or twisting angles can trigger the snap-folding, the different mechanisms lead to different subsequent folding paths (Figs. 2(b) and 2(d) for comparison). These folding mechanisms applied to 2D and 3D structures will be further explored next as the advantages of single hexagonal rings are extended to various assemblies.

**Folding of Hexagonal Ring Assemblies Via Method of Stacking.** Individual hexagonal rings can be used as building blocks to construct assemblies that can achieve tremendous packing ratios upon folding. Here, 2D and 3D ring assemblies are introduced, including 2D tessellation, a 3D dome structure, and a reconfigurable 3D box. As shown in Fig. 3(a), six hexagonal rings are assembled into a 2D radial pattern, resulting in an enclosed structure whose center has the shape of a hexagon. Adjacent edges between hexagons are connected by tape hinges, which allow for relative rotation between the edges while constraining their relative translational motion. Following the path in Fig. 3(b), the rings can

be stacked into six fully overlapping hexagonal rings, which are then folded by twisting to reach the folded configuration, thereby leading to 1.5% of the initial area of the deployed 2D tessellation (see Movie 2 available in the Supplemental Materials on the ASME Digital Collection). This folding process is reversible by un-folding the overlapping peach core structure back to the six overlapping hexagonal rings, followed by un-stacking. In addition to 2D assemblies, a similar stacking process can be performed for 3D assemblies. As shown in Fig. 3(c), five hexagonal rings connected at their edges with tape hinges and one detachable hinge are assembled to create a dome-like structure. The detachable hinge allows for the disassembly of the 3D structure into a 2D one with five hexagonal rings patterned in a radial manner (Fig. 3(d)). From here, a similar stacking process proceeds as before, where the rings are stacked to five fully overlapping hexagonal rings, which are then folded via twisting, resulting in a folded state possessing only 0.4% of the initial volume (see Movie 2 available in the Supplemental Materials on the ASME Digital Collection). Similarly, these folded rings can re-deploy to the five stacked rings, and the dome structure can be recovered by un-stacking and re-attaching the rings.

In Fig. 3(e), a 3D box structure is introduced, which is both foldable and reconfigurable. The box is composed of four hexagonal rings connected to each other by tape hinges. To fold the box, two opposite corners of the box are pulled aside to flatten the structure, resulting in a 2D configuration of the four rings (Fig. 3(f)). These rings are then stacked to four fully overlapping rings and

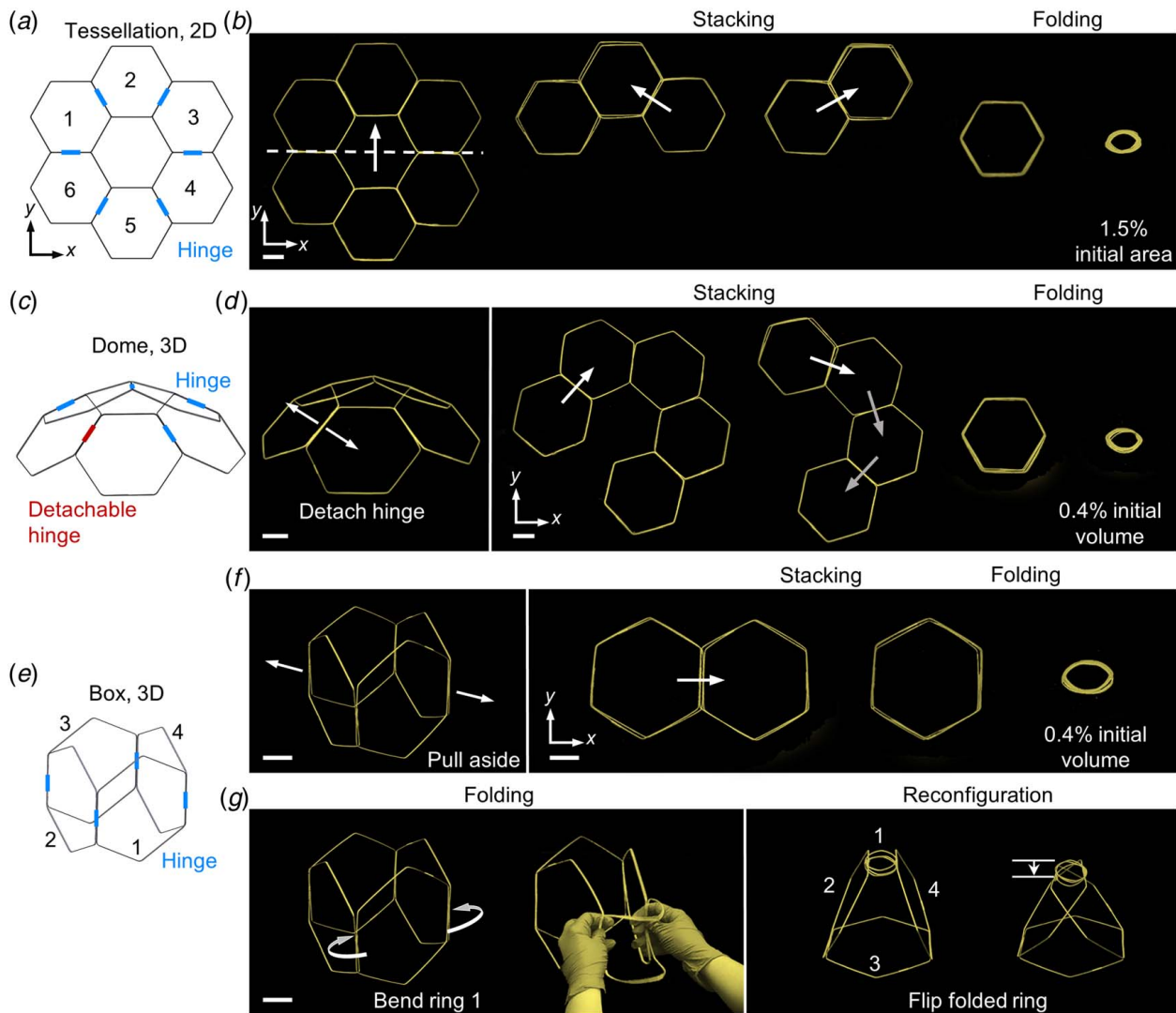


**Fig. 3** Experimental folding process of hexagonal ring assemblies with extreme packing via stacking and snap-folding. (a) Assembly schematic of 2D tessellation with six hexagonal rings, (b) experimental images of the stacking and folding process of the 2D tessellation, (c) assembly schematic of a 3D dome made of five hexagonal rings, (d) experimental images of the detaching, stacking, and folding process of the dome, (e) assembly schematic of a 3D box made of four hexagonal rings, (f) experimental images of the stacking and folding process of the box, and (g) reconfiguration process of the box. Scale bars: 5 cm. (Color version online.)

then snap-folded to a folded state with 0.4% of the initial volume (see Movie 3 available in the Supplemental Materials on the ASME Digital Collection). These rings can be re-deployed to the original configuration by reversing the steps taken to fold the box. Figure 3(g) demonstrates an alternative method to fold the box, in which it is reconfigured by selectively folding a single ring of the box. The front ring (ring 1) of the box is folded by applying bending loads (white arrows) to the hinged edges of the ring (See Fig. S3 available in the Supplemental Materials on the ASME Digital Collection for single ring folding by bending hexagonal ring edges). As the ring folds, the two hinged edges of ring 1 are brought closer together, leading to a reconfigured structure resembling a pyramid. It can be further reconfigured by flipping the folded ring 1. In this process, rings 2 and 4 crosses and the structure decreases in height, for a shorter pyramid-like structure (see Movie 3 available in the Supplemental Materials on the ASME Digital Collection). The structure can return to the initial box by flipping and un-folding ring 1. The reconfigurable box assembly demonstrates the versatility of ring assemblies; reversible global shape change can be achieved by selectively folding individual rings of a given structure.

**Direct Folding of 3D Ring Assemblies and Their Stability.** Besides stacking and folding, assemblies that can fold directly from their 3D configuration to states with largely reduced volume are achievable. Further, the mechanical stability of 3D structures can be tuned by adjusting the stability of individual rings. The main parameters that affect ring foldability and folded ring stability are the cross section and the corner radius of the ring [36]. Since the cross section of the rings in this work is held constant, we will only focus on changing the corner radius for varying the mechanical stability. As shown in Fig. 4(a),  $r$  denotes the radius of the corners of the hexagonal ring, and  $a$  denotes the edge length or the length between the adjacent corners. In Fig. 4(b), the FEA results illustrate the folding process for two rings, one with a relatively large radius  $r/a=0.3$  and one with a relatively small radius  $r/a=0.05$ , respectively. Their foldability and stability are evaluated by assessing the normalized moment versus twisting angle. Here, the normalized moment is  $Ma/EJ$ , where  $E$  is the Young's modulus of the ring material and  $J$  is the torsional constant of the ring cross section (See Supplemental Materials on the ASME Digital Collection for the calculation of  $J$ ). For snap-folding of single rings via twisting, the moment gradually increases and then gradually drops until

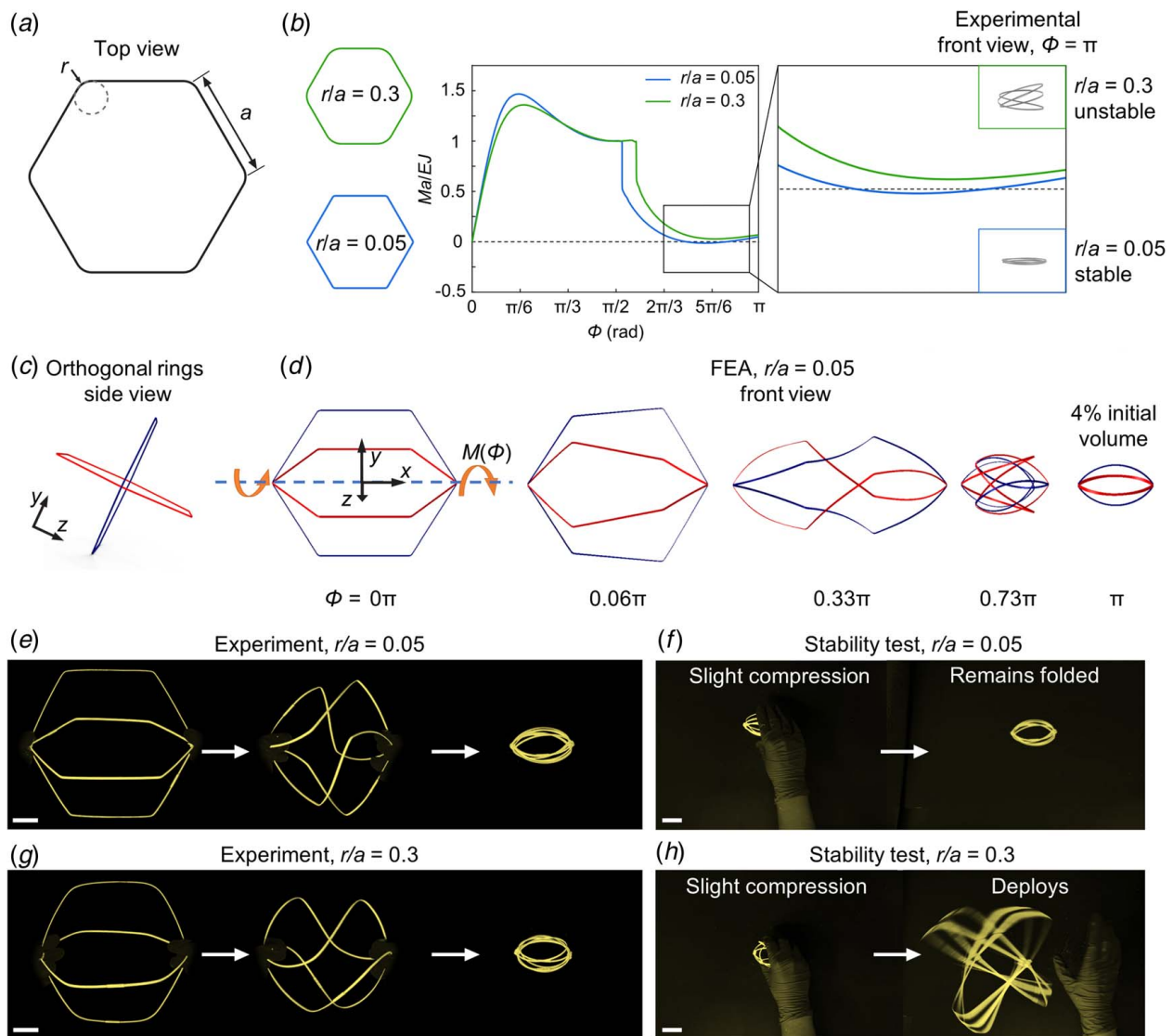


**Fig. 4** FEA simulation and experimental validation of the tunable stability of hexagonal rings and their assemblies. (a) Schematic of the hexagonal ring along with geometric parameters, (b) schematic top views of two selected ring geometries, and FEA results of the normalized moment versus twisting angle graph for rings with different corner radii. Black boxed region of the graph is enlarged, with corresponding experimental folded front views of selected ring geometries shown. (c) Assembly schematic side view of two orthogonal rings, (d) FEA results of folding a  $r/a = 0.05$  orthogonal ring assembly by twisting. Experimental images of (e) folding process and (f) stability test of the  $r/a = 0.05$  ring assembly. Experimental images of (g) folding process and (h) stability test of the  $r/a = 0.3$  ring assembly. Scale bars: 2.5 cm. (Color version online.)

reaching the snapping point, after which the moment abruptly drops towards zero. For the geometries whose normalized moment drops to zero, the folded configuration is stable. As seen in the enlarged portion of the graph in Fig. 4(b), the  $r/a = 0.3$  ring (green curve) maintains a normalized moment greater than zero, whereas the  $r/a = 0.05$  curve (blue) drops below zero. Thus, the folded state of the  $r/a = 0.3$  ring is considered unstable and that of the  $r/a = 0.05$  ring to be stable (See Fig. S4 available in the Supplemental Materials on the ASME Digital Collection for more information on the stability of hexagonal rings under twisting upon varying the  $r/a$  value). The front views of the folded rings from experiments are shown to the right in Fig. 4(b), where the  $r/a = 0.3$  ring has an unstable 3D folded state held together by the surface friction of the looped ring (See Fig. S5 available in the Supplemental Materials on the ASME Digital Collection for single  $r/a = 0.3$  hexagonal ring folding process). On the other hand, the  $r/a = 0.05$  ring has a stable 2D folded state, in agreement with the FEA results.

To further exploit these differences in stability for 3D application, two rings are assembled in an orthogonal manner (a side

view schematic of this assembly is shown in Fig. 4(c)). This results in a ball-like truss structure, which has variable folded stability depending on the  $r/a$  values of the rings used. The rings are connected to each other at opposing corners, wound by rubber bands, which restrict relative translational motion, while still maintaining an overall orthogonal arrangement. In FEA, the twisting angle  $\Phi$  (indicated by orange arrows) is applied to the connected corners in opposing directions about the  $x$ -axis (blue dotted line), with the twisting moment designated by  $M$ , as shown in Fig. 4(d). The folding process of the structure with  $r/a = 0.05$  rings is shown at various twisting angles. Throughout the process, the connected corners translate inward along the  $x$ -axis and the two rings fold simultaneously until a fully folded configuration is reached at  $\Phi = \pi$  (see Movie 4 available in the Supplemental Materials on the ASME Digital Collection). Note that the folded configuration is 3D and has a shape similar to an American football, with a folded volume of only 4% of the initial volume. To experimentally validate the folding and stability of this structure, two  $r/a = 0.05$  rings are assembled and twisting angles in opposing

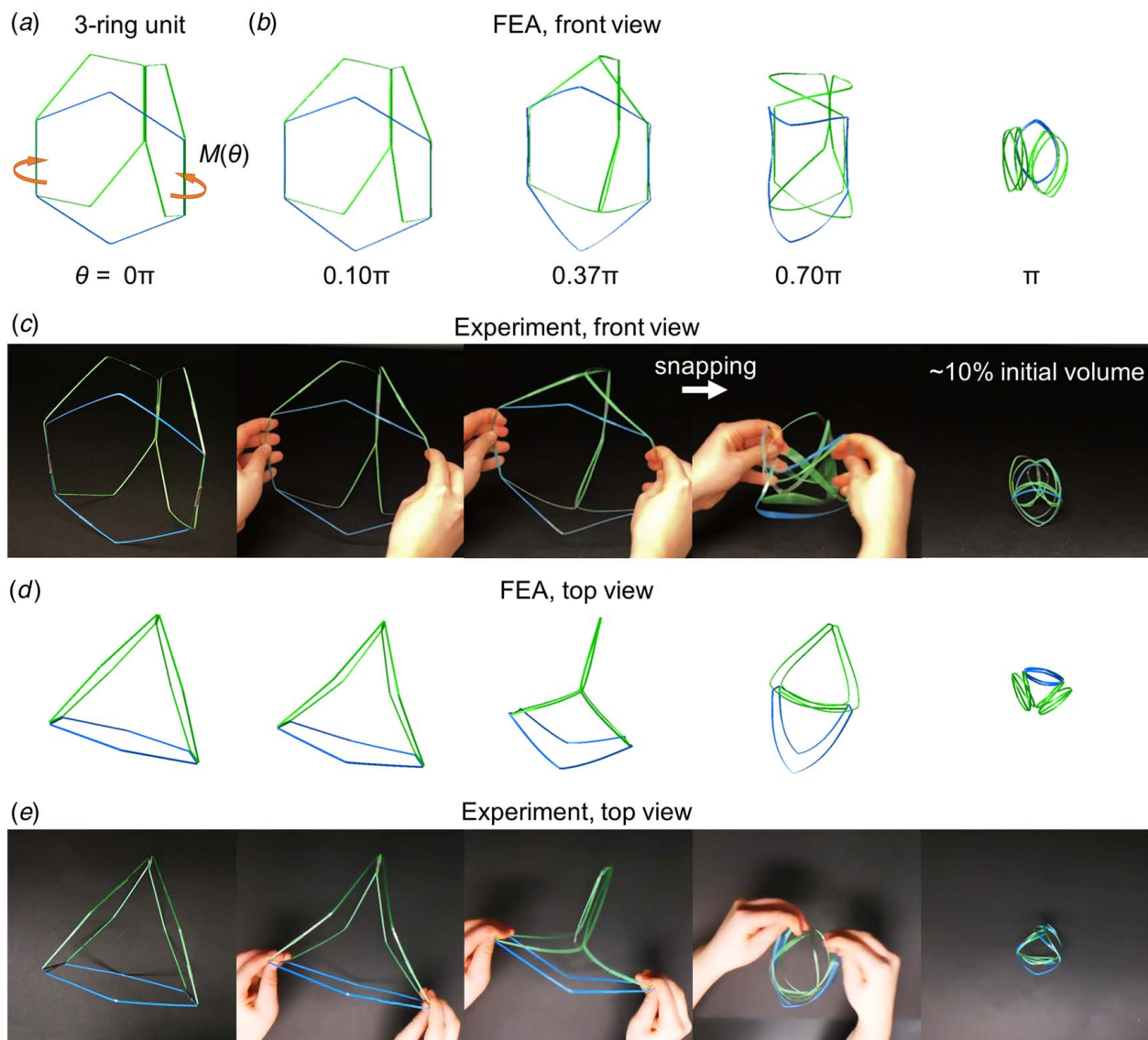


**Fig. 5 Simultaneous bending-induced snap-folding of a 3-ring unit. (a) Schematic of the unit under twisting. Front view of the folding process of the 3-ring unit in (b) FEA and (c) experiment. Top view of the folding process of the 3-ring unit in (d) FEA and (e) experiment. (Color version online.)**

directions are applied to both ends, as shown in Fig. 4(e), where the experimental configurations match well with those from FEA. To test the stability of the folded state, a slight compression is applied to the structure and released, after which the rings remain in their folded configuration (Fig. 4(f)), as expected. Note that this structure is easily deployed to its initial state by applying reverse twisting on the two corners which were previously twisted. Next, another orthogonal ring structure is assembled and folded with rings of  $r/a = 0.3$  (Fig. 4(g), see Fig. S6 available in the Supplemental Materials on the ASME Digital Collection for FEA validation). The same stability test is applied to the folded  $r/a = 0.3$  structure, however, this time the structure snap-deploys after the slight compression, indicating that it is unstable (Fig. 4(h), see Movie 4 available in the Supplemental Materials on the ASME Digital Collection). By taking advantage of the inherent stability differences among different ring geometries, the mechanical stabilities of structures can be tuned. Further, the instabilities of rings can be utilized to facilitate the automatic deployment of folded ring assemblies when small perturbations are applied (see Movie 4 available in the Supplemental Materials on the ASME Digital Collection).

**Folding 3D Ring Assemblies Upon Local Actuation.** For the folding of complicated large structures, it is desirable to obtain global deformation through local actuation. Here, we demonstrate this through a “3-ring unit” of hexagonal rings, which exhibits global deformation triggered by local actuation. For this structure, the three rings are assembled, connected to each other at the center of adjacent edges with tape, with an initial 60 deg angle between adjacent rings. As shown in Fig. 5(a), bending angles are applied to the center of the hinged edges of the blue front ring, thereby leading to an outward bending of the ring. This simultaneously results in two pairs of bending loads on the adjacent two green rings for inward bending, which collapses the whole structure by snap-folding all three rings concurrently. Figure 5(b) shows the front view of the FEA simulation of the folding process, with the bending angle starting from 0 and ending at  $\pi$ . Throughout folding, there exists relative rotation between rings which is allowed by the tape joints. Figure 5(c) shows the front view of the experimental folding process (see Movie 5 available in the Supplemental Materials on the ASME Digital Collection). The final 3D folded structure has only  $\sim 10\%$  of the initial structural volume. Figures 5(d) and 5(e) show FEA and experimental top views of

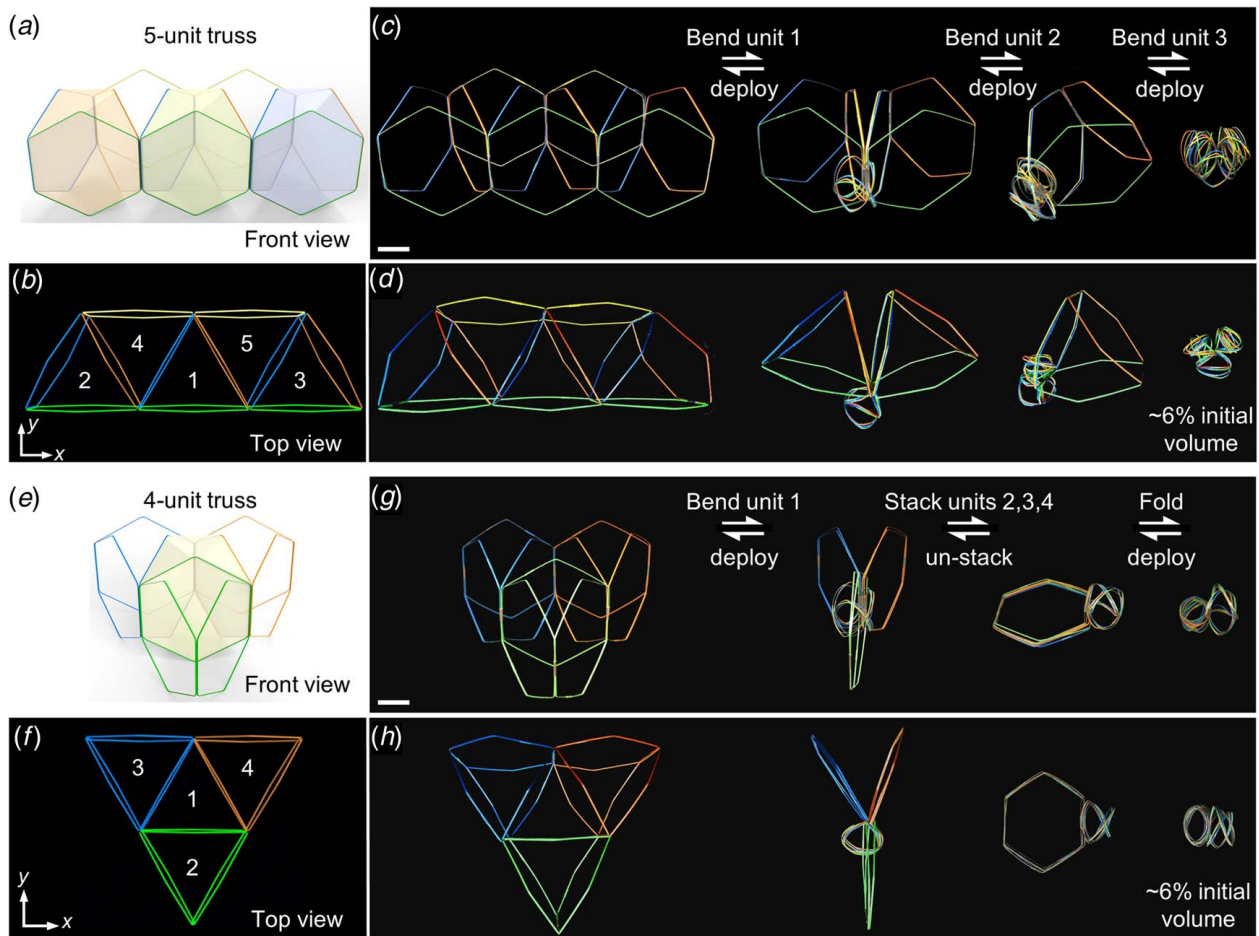


**Fig. 6** Reconfigurable truss structures composed of 3-ring units for tremendous volume packing. (a) Assembly schematic of a 5-unit truss, front view, (b) assembly schematic of 5-unit truss, with units numbered, top view, (c) experimental images of the folding process of the 5-unit truss, front view, (d) experimental images of the folding process of the 5-unit truss, top view, (e) assembly schematic of a 4-unit truss, front view, (f) assembly schematic of a 4-unit truss, with units numbered, top view, (g) experimental images of the folding process of the 4-unit truss, front view, and (h) experimental images of the folding process of the 4-unit truss, top view. Scale bar: 5 cm. (Color version online.)

the folding process, respectively. The experiment and FEA match well for the beginning of the folding process, but differences between the experiment and FEA arise later in the folding process, mainly due to the interpenetration of rings which is allowed in the FEA simulation.

By creating assemblies with the 3-ring units as the basic building blocks, truss structures with more significant volume packing and various intermediate reconfigured structures are achievable. As seen in Fig. 6(a), a truss made of five units is constructed, where rings adjacent to one another are connected at the middle of their edges by tape. Note here that each of these five units shares at least one hexagonal ring with an adjacent unit. The shaded orange (left), yellow (middle), and blue (right) units in the schematic in Fig. 6(a) illustrate those to be bent during the folding process. Figure 6(b) shows a top view of the truss, with each unit assigned a number. Folding this structure to its final configuration with a largely reduced volume involves three bending steps (see Movie 6 available in the Supplemental Materials on the ASME Digital Collection). First, bending angles applied to the center edges of the green (front) ring of the middle unit (unit 1) lead to the folding of the unit (second configuration, Figs. 6(c) and 6(d)). At the same time, the two yellow rings in the back of the structure collapsed onto the orange ring of unit 2 and the blue ring of unit 3, respectively. Thus, there remain two deployed units after the first step in the folding process. Note that all steps in the entire process are reversible (indicated by white arrows) by simply

reversing the folding steps. Next, as shown in Figs. 6(c) and 6(d), the left unit (unit 2) is bent at the edges of the blue ring. The resulting configuration (third configuration, Figs. 6(c) and 6(d)) is a single deployed unit with two folded units attached. This structure is folded to its final configuration by applying bending loads to the edges of the orange ring of the remaining unit (see Movie 6 available in the Supplemental Materials on the ASME Digital Collection). The final folded structure has a volume that is only  $\sim 6\%$  of the initial deployed volume.

Figure 6(e) shows another truss design by assembling four 3-ring units into a triangular prism configuration. The outer units are made of green (front unit), blue (back left unit), and orange (back right unit) rings, and the central unit (shaded in yellow) is composed of one ring of each color. A top view of this structure is shown in Fig. 6(f), where the central unit is designated as unit 1 and the surrounding units are designated as 2, 3, and 4. Similar to the earlier truss, the folding process is initiated by applying bending loads to the center edges of the green ring of the middle unit (unit 1), after which the immediate adjacent units collapse (second configuration, Figs. 6(g) and 6(h)). The resulting reconfigured structure is the folded unit 1 connected to the collapsed units 2, 3, and 4. Note that these “collapsed units” are the two outermost rings of each unit. The collapsed units are then stacked together, as shown in the third configuration of Figs. 6(g) and 6(h). Twisting loads are applied to these stacked rings to reach the ultimate folded configuration, shown in Figs. 6(g) and 6(h) (see Movie 6 available in the

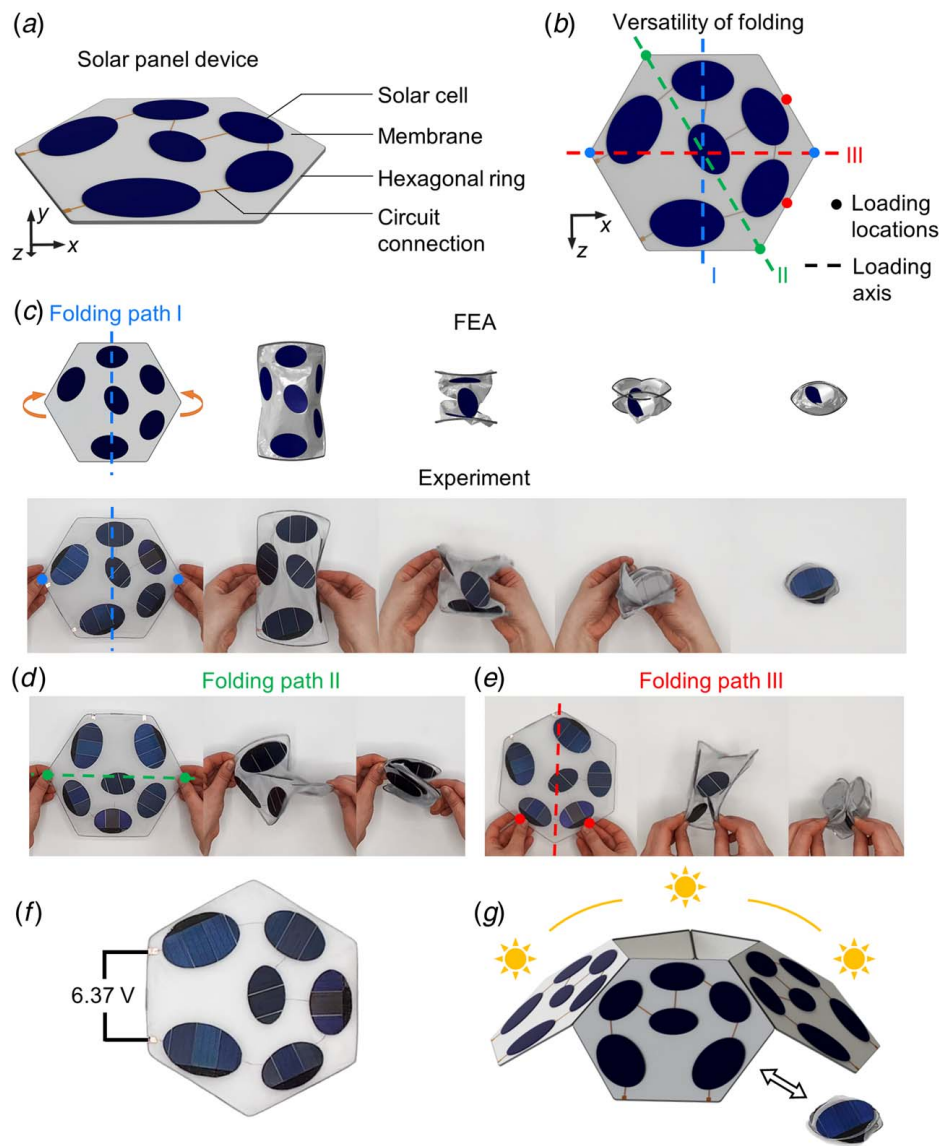


**Fig. 7 Functional hexagonal ring assembly with rigid solar panels and versatile folding capabilities. (a) Assembly schematic of the circuit for the solar panel device, (b) three distinct folding paths (I, II, and III) and their loading locations, (c) FEA (top row) and experimental (bottom row) results of folding process along folding path I, (d) experimental folding process along folding path II, (e) experimental folding process along folding path III, (f) experimental voltage measurement of the device in sunlight, and (g) assembly schematic of a dome structure with rigid solar panels. (Color version online.)**

Supplemental Materials on the ASME Digital Collection). The final volume is only  $\sim 6\%$  of the initial deployed truss volume and the 4-unit truss can be deployed to its initial configuration by reversing the folding process. With extended truss structures that have tremendous volume packing ratios, it is anticipated that these assemblies could inspire future deployable structure design.

**Ring Folding With Functional Rigid Solar Panels.** Although hexagonal rings show superior packing capabilities, the demonstrations aforementioned only illustrate the structural transformations achievable through the snap-folding of hexagonal rings. To further take advantage of the folding capabilities of hexagonal rings, we integrate rigid functional components with the ring via a flexible membrane for functional devices. A solar panel device is demonstrated, as shown in Fig. 7(a). The assembly is a hexagonal ring with thin membrane (light gray) attached, on top of which a circuit of six elliptical solar panels (dark blue) is adhered. The

solar panels are connected in series by copper wire. Despite the rigid nature of the solar panels, the rationally designed distribution of panels allows for uninhibited snap-folding of the device. As shown in Fig. 7(b), the solar panel device allows for versatility of folding, with three distinct folding paths achievable based on different loading locations (green, red, and blue dots) and their corresponding loading axes (green, red, and blue dotted lines). Folding path I, a bending-induced snap-folding process, is achievable by applying bending angles (orange arrows) about the blue axis, at the corners located on the central horizontal line of the ring in Fig. 7(c). As the corners translate inwards, the ring guides the movement of the membrane and the panels subsequently help guide the folding path, enabling the overlap of panels throughout the folding process (see Movie 7 available in the Supplemental Materials on the ASME Digital Collection). The folded state has roughly 11% of the initial area of the deployed device. Both FEA (top row) and experimental (bottom row) results of this folding process are shown in Fig. 7(c), showing good agreement with one another.

Folding path II, a twisting-induced snap-folding process, is achieved by applying twisting angles to the corners running through the green axis indicated in Figs. 7(b) and 7(d). Lastly, folding path III is achieved by application of bending about the red axis indicated in Figs. 7(b) and 7(e), with corresponding loading locations indicated by red dots. Due to the rationally designed panel distribution, despite different loads being applied about different axes, the panels guide the folding paths to the same final folded state with the same organization of overlapped panels (see Movie 7 available in the Supplemental Materials on the ASME Digital Collection). The device can be easily deployed back to its initial state by applying reversed twisting or bending loads at the locations where folding was initiated. This reliably foldable and deployable device can lend itself to use as a portable charger, with a voltage reading of 6.37 V in sunlight when solar irradiance is  $\sim 900 \text{ W/m}^2$  (Fig. 7(f)). The compactness of the folded device allows for easy storage (See Fig. S7 available in the Supplemental Materials on the ASME Digital Collection), showing promise as a portable device with great packing and versatility. For future application, foldable structures with integrated functional rigid components such as the dome schematic shown in Fig. 7(g) are possible, which could take advantage of incident sunlight from different directions throughout the day. It should be noted that future assemblies can be further optimized by incorporating additional rigid or soft functional components with membrane and hexagonal ring. By illustrating the compatibility of rigid functional components with the snap-folding of hexagonal rings, we anticipate that this concept could be expanded to future deployable aerospace or electronics applications.

## Discussion

In this work, we study 2D and 3D hexagonal ring assemblies that pack to significantly reduced areas and volumes upon folding. While the individual hexagonal ring folds to 10.6% of its deployed area, the packing capabilities of individual rings can be expanded to various designed 2D and 3D assemblies to result in structures that fold to as low as 1.5% and 0.4% of their initial area and volume, respectively. Based on the experimental and FEA results, structures that can directly fold from their 3D configurations are demonstrated and the tunable mechanical stability of folded assemblies, as well as the global deformation of assemblies upon local actuation, are explored. Additionally, rigid functional components can be integrated with hexagonal rings for devices or structures with versatile, repeatable folding. We anticipate that the tremendous packing of 2D and 3D hexagonal ring assemblies, as well as the versatility enabled by folding will inspire the design of future deployable structures.

## Materials and Methods

**Ring and Assembly Fabrication.** Hexagonal rings were made from stainless steel rods (See Figs. S8 and S9 available in the Supplemental Materials on the ASME Digital Collection for information on the maximum strain of the ring during bending or twisting and ring design considerations for the avoidance of plasticity) of rectangular cross section with height of 2.0 mm and thickness of 0.50 mm. All hexagonal rings used in the demonstrations had an edge length of 100 mm and corner radius of 5 mm, except for the  $r/a = 0.3$  orthogonal ring assembly, which utilized rings with a corner radius of 30 mm. A commercial acrylic paint was applied to the rings to aid in visualization. Rings in assemblies from Figs. 3, 5, and 6 were attached together with tape. The five-ring dome assembly utilized two magnets, both connected to one edge of a ring to serve as the detachable hinge. The orthogonally arranged rings from Fig. 4 were connected at the corners, wound together by rubber bands. The solar panel device from Fig. 7 was fabricated by gluing a thin, flexible fabric to the ring, to serve as the membrane. Commercial solar panels were cut into elliptical shapes of specified size and connected in series via

soldering with copper wire. The circuit was then glued to the membrane. See Fig. S10 available in the Supplemental Materials on the ASME Digital Collection for details on area and volume packing calculations for all assemblies.

**Finite Element Analysis Simulation.** Snap-folding simulations of hexagonal rings and hexagonal ring assemblies were done with the commercial software ABAQUS 2019 (Dassault Systèmes, France). For all simulations, the C3D8R element was used with linear elastic material with  $E = 200 \text{ GPa}$  and Poisson's ratio of 0.3. A damping factor of  $10^{-10}$  was used to stabilize all simulations and self-contact was not considered during the folding processes.

**Single ring and orthogonal rings FEA:** Boundary conditions were applied at loading locations to reference points which were constrained with nodes of the cross section using multipoint constraints (MPCs). Rotation of  $\pi$  was applied to the reference points at the left and right corners of the ring in reverse directions. For single ring twisting and twisting of orthogonal ring structures with  $r/a = 0.05$ , additional small forces were applied at the reference points to push the corners inwards to trigger the snap-folding.

**3-Ring unit folding FEA:** The three rings were constrained together by connecting the center points of the coincident edges via MPCs. Rotation of  $\pi$  was applied to the reference points at the left and right edges of the front blue ring in reverse directions. Additional small forces were applied to the free top and bottom corners of the two green rings to push the corners inwards, which helps trigger the simultaneous bending-induced snap-folding.

**Hexagonal ring assembly with rigid panels FEA:** To account for the differences in material stiffness of the different components of the assembly, the much softer fabric had Young's modulus ratio of 1/10,000 to the ring material, while the solar panels had a Young's modulus ratio of 1/100 to the ring material. A Poisson's ratio of 0.3 was chosen for all materials. The same boundary conditions used for bending of a single ring were adopted.

## Author Contribution Statement

Conceptualization: SL, SW, JD, RRZ  
 Methodology: SL, SW, JD, RRZ  
 Investigation: SL, SW, JD  
 Visualization: SL, SW, JD, RRZ  
 Supervision: RRZ  
 Writing—original draft: SL, RRZ  
 Writing—review & editing: SL, SW, JD, RRZ

## Funding Data

- National Science Foundation (NSF) (Award No. EFMA-2029643; Funder ID: 10.13039/501100008982 (SW and RRZ)).
- National Science Foundation (NSF) (Career Award No. CMMI-2145601; Funder ID: 10.13039/501100008982 (SL, SW, JD, and RRZ)).
- National Science Foundation (NSF) (Award No. CMMI-2142789; Funder ID: 10.13039/501100008982 (SL, SW, JD, and RRZ)).

## Conflict of Interest

There are no conflicts of interest.

## Data Availability Statement

The authors attest that all data for this study are included in the paper.

## References

- [1] Zirbel, S. A., Lang, R. J., Thomson, M. W., Sigel, D. A., Walkemeyer, P. E., Trease, B. P., Magleby, S. P., and Howell, L. L., 2013, "Accommodating Thickness in Origami-Based Deployable Arrays," *ASME J. Mech. Des.*, **135**(11), p. 111005.
- [2] Chen, T., Bilal, O. R., Lang, R., Daraio, C., and Shea, K., 2019, "Autonomous Deployment of a Solar Panel Using Elastic Origami and Distributed Shape-Memory-Polymer Actuators," *Phys. Rev. Appl.*, **11**(6), p. 064069.
- [3] Kuribayashi, K., Tsuchiya, K., You, Z., Tomus, D., Umamoto, M., Ito, T., and Sasaki, M., 2006, "Self-Deployable Origami Stent Grafts as a Biomedical Application of Ni-Rich TiNi Shape Memory Alloy Foil," *Mater. Sci. Eng. A*, **419**(1), pp. 131–137.
- [4] Wu, S., Ze, Q., Dai, J., Udupi, N., Paulino, G. H., and Zhao, R., 2021, "Stretchable Origami Robotic Arm With Omnidirectional Bending and Twisting," *Proc. Natl. Acad. Sci.*, **118**(36), p. e2110023118.
- [5] Lahikainen, M., Zeng, H., and Priimagi, A., 2018, "Reconfigurable Photoactuator Through Synergistic Use of Photochemical and Photothermal Effects," *Nat. Commun.*, **9**(1), p. 4148.
- [6] Wu, S., Ze, Q., Zhang, R., Hu, N., Cheng, Y., Yang, F., and Zhao, R., 2019, "Symmetry-Breaking Actuation Mechanism for Soft Robotics and Active Metamaterials," *ACS Appl. Mater. Interfaces*, **11**(44), pp. 41649–41658.
- [7] Kamrava, S., Mousanezhad, D., Ebrahimi, H., Ghosh, R., and Vaziri, A., 2017, "Origami-Based Cellular Metamaterial With Auxetic, Bistable, and Self-Locking Properties," *Sci. Rep.*, **7**(1), p. 46046.
- [8] Iniguez-Rabago, A., Li, Y., and Overvelde, J. T. B., 2019, "Exploring Multi-Stability in Prismatic Metamaterials Through Local Actuation," *Nat. Commun.*, **10**(1), p. 5577.
- [9] Jenett, B., Cameron, C., Tourlomis, F., Rubio, A. P., Ochalek, M., and Gershenfeld, N., 2020, "Discretely Assembled Mechanical Metamaterials," *Sci. Adv.*, **6**(47), p. eabc9943.
- [10] Melancon, D., Gorissen, B., García-Mora, C. J., Hoberman, C., and Bertoldi, K., 2021, "Multi-Stable Inflatable Origami Structures at the Metre Scale," *Nature*, **592**(7855), pp. 545–550.
- [11] Alegria Mira, L., Thrall, A. P., and De Temmerman, N., 2014, "Deployable Scissor Arch for Transitional Shelters," *Autom. Constr.*, **43**, pp. 123–131.
- [12] Choi, G. P. T., Dudte, L. H., and Mahadevan, L., 2019, "Programming Shape Using Kirigami Tessellations," *Nat. Mater.*, **18**(9), pp. 999–1004.
- [13] Filipov, E. T., Tachi, T., and Paulino, G. H., 2015, "Origami Tubes Assembled Into Stiff, Yet Reconfigurable Structures and Metamaterials," *Proc. Natl. Acad. Sci.*, **112**(40), pp. 12321–12326.
- [14] Mao, Y., Yu, K., Isakov, M. S., Wu, J., Dunn, M. L., and Jerry Qi, H., 2015, "Sequential Self-Folding Structures by 3D Printed Digital Shape Memory Polymers," *Sci. Rep.*, **5**(1), p. 13616.
- [15] Kuang, X., Wu, S., Ze, Q., Yue, L., Jin, Y., Montgomery, S. M., Yang, F., Qi, H. J., and Zhao, R., 2021, "Magnetic Dynamic Polymers for Modular Assembling and Reconfigurable Morphing Architectures," *Adv. Mater.*, **33**(30), p. 2102113.
- [16] Wang, W., Kim, N.-G., Rodrigue, H., and Ahn, S.-H., 2017, "Modular Assembly of Soft Deployable Structures and Robots," *Mater. Horiz.*, **4**(3), pp. 367–376.
- [17] Liu, F., Jiang, X., Wang, X., and Wang, L., 2020, "Machine Learning-Based Design and Optimization of Curved Beams for Multi-Stable Structures and Metamaterials," *Extreme Mech. Lett.*, **41**, p. 101002.
- [18] Mhatre, S., Boatti, E., Melancon, D., Zareei, A., Dupont, M., Bechthold, M., and Bertoldi, K., 2021, "Deployable Structures Based on Buckling of Curved Beams Upon a Rotational Input," *Adv. Funct. Mater.*, **31**(35), p. 2101144.
- [19] Dudte, L. H., Vouga, E., Tachi, T., and Mahadevan, L., 2016, "Programming Curvature Using Origami Tessellations," *Nat. Mater.*, **15**(5), pp. 583–588.
- [20] Liu, K., Han, L., Hu, W., Ji, L., Zhu, S., Wan, Z., Yang, X., et al., 2020, "4D Printed Zero Poisson's Ratio Metamaterial With Switching Function of Mechanical and Vibration Isolation Performance," *Mater. Des.*, **196**, p. 109153.
- [21] Tao, R., Xi, L., Wu, W., Li, Y., Liao, B., Liu, L., Leng, J., and Fang, D., 2020, "4D Printed Multi-Stable Metamaterials With Mechanically Tunable Performance," *Compos. Struct.*, **252**, p. 112663.
- [22] Rafsanjani, A., Akbarzadeh, A., and Pasini, D., 2015, "Snapping Mechanical Metamaterials Under Tension," *Adv. Mater.*, **27**(39), pp. 5931–5935.
- [23] Tian, D., Guo, Z., Jin, L., Zhang, K., Gao, H., Fan, X., and Liu, Z., "Design and Deployment Experiment Research on Support Mechanism for Hexagonal Prism Modular Deployable Antenna," 2021 IEEE 4th International Conference on Electronics Technology (ICET), Chengdu, China, May 7–10, pp. 627–631.
- [24] Gardner, J. P., Mather, J. C., Clampin, M., Doyon, R., Greenhouse, M. A., Hammel, H. B., Hutchings, J. B., et al., 2006, "The James Webb Space Telescope," *Space Sci. Rev.*, **123**(4), pp. 485–606.
- [25] Grumman, N., and Gunn, C., 2020, "Successful Mirror Deployment Test," for the First Time," Photograph, <https://www.flickr.com/photos/nasawebtelescope/49754454197/in/album-72157691368095482/>
- [26] Gunn, C., 2019, "NASA's James Webb Space Telescope Has Been Assembled for the First Time," Photograph, <https://www.flickr.com/photos/nasawebtelescope/48636487363/in/album-72157691368095482/>
- [27] Sahr, K., White, D., and Kimerling, A. J., 2003, "Geodesic Discrete Global Grid Systems," *Cartogr. Geogr. Inf. Sci.*, **30**(2), pp. 121–134.
- [28] Zhao, Z., Wang, K., Zhang, L., Wang, L.-C., Song, W.-L., and Fang, D., 2019, "Stiff Reconfigurable Polygons for Smart Connectors and Deployable Structures," *Int. J. Mech. Sci.*, **161–162**, p. 105052.
- [29] Zhang, Y.-J., Wang, L.-C., Song, W.-L., Chen, M., and Fang, D., 2020, "Hexagon-Twist Frequency Reconfigurable Antennas Via Multi-Material Printed Thermo-Responsive Origami Structures," *Front. Mater.*, **7**, pp. 1–11.
- [30] Yan, Z., Zhang, F., Wang, J., Liu, F., Guo, X., Nan, K., Lin, Q., et al., 2016, "Controlled Mechanical Buckling for Origami-Inspired Construction of 3D Microstructures in Advanced Materials," *Adv. Funct. Mater.*, **26**(16), pp. 2629–2639.
- [31] Li, S., Deng, B., Grinthal, A., Schneider-Yamamura, A., Kang, J., Martens, R. S., Zhang, C. T., et al., 2021, "Liquid-Induced Topological Transformations of Cellular Microstructures," *Nature*, **592**(7854), pp. 386–391.
- [32] Overvelde, J. T. B., Weaver, J. C., Hoberman, C., and Bertoldi, K., 2017, "Rational Design of Reconfigurable Prismatic Architected Materials," *Nature*, **541**(7637), pp. 347–352.
- [33] Chen, Y., You, Z., and Tarnai, T., 2005, "Threefold-Symmetric Bricard Linkages for Deployable Structures," *Int. J. Solids Struct.*, **42**(8), pp. 2287–2301.
- [34] Gao, W., Huo, K., Seehra, J. S., Ramani, K., and Cipra, R. J., "HexaMorph: A Reconfigurable and Foldable Hexapod Robot Inspired By Origami," 2014 IEEE/RSJ International Conference on Intelligent Robots and Systems, Chicago, IL, Sept. 14–18, pp. 4598–4604.
- [35] Wu, S., Yue, L., Jin, Y., Sun, X., Zemelka, C., Qi, H. J., and Zhao, R., 2021, "Ring Origami: Snap-Folding of Rings With Different Geometries," *Adv. Intell. Syst.*, **3**(9), p. 2100107.
- [36] Wu, S., Dai, J., Leanza, S., and Zhao, R. R., 2022, "Hexagonal Ring Origami—Snap-Folding With Large Packing Ratio," *Extreme Mech. Lett.*, **53**, p. 101713.